

Instruments and Methods

Geophysical imaging of alpine rock glaciers

Hansruedi MAURER,¹ Christian HAUCK²

¹*Institute of Geophysics, ETH-Hönggerberg, CH-8093 Zürich, Switzerland*

E-mail: maurer@aug.ig.erdw.ethz.ch

²*Institute for Meteorology and Climate Research, Forschungszentrum Karlsruhe/University of Karlsruhe, Postfach 3460, D-76021 Karlsruhe, Germany*

ABSTRACT. Slope instabilities caused by the disappearance of ice within alpine rock glaciers are an issue of increasing concern. Design of suitable counter-measures requires detailed knowledge of the internal structures of rock glaciers, which can be obtained using geophysical methods. We examine benefits and limitations of diffusive electromagnetics, geoelectrics, seismics and ground-penetrating radar (georadar) for determining the depth and lateral variability of the active layer, the distributions of ice and water, the occurrence of shear horizons and the bedrock topography. In particular, we highlight new developments in data acquisition and data analysis that allow 2-D or even 3-D structures within rock glaciers to be imaged. After describing peculiarities associated with acquiring appropriate geophysical datasets across rock glaciers and emphasizing the importance of state-of-the-art tomographic inversion algorithms, we demonstrate the applicability of 2-D imaging techniques using two case studies of rock glaciers in the eastern Swiss Alps. We present joint interpretations of geoelectric, seismic and georadar data, appropriately constrained by information extracted from boreholes. A key conclusion of our study is that the different geophysical images are largely complementary, with each image resolving a different suite of subsurface features. Based on our results, we propose a general template for the cost-effective and reliable geophysical characterization of mountain permafrost.

1. INTRODUCTION

Permafrost underlies most polar and many mountainous regions of the Earth. A significant portion of permafrost in the European Alps, which is commonly found above ~2500 m altitude, exists in the form of rock glaciers. These amalgamations of boulders, unconsolidated sediments, ice, water and air form on gently to moderately dipping mountain slopes. Other distinct mountain permafrost features include ice-cored moraines, protalus ramparts and scree slopes (Kneisel, 2004).

In many populated mountain areas, permafrost impacts on a number of hazard-relevant issues. For example, the frozen nature of the ground is essential for the stability of certain critical constructions, such as avalanche protectors, power poles and cable-car installations (Haeberli, 1992). Moreover, the stability of numerous mountain areas is largely controlled by the presence of ice (Davies and others, 2001).

Since the temperature of most mountain permafrost is close to the freezing point, it is susceptible to small changes in climate. It is therefore not surprising that during the past few decades, thawing of permafrost, probably caused by global warming, has resulted in catastrophic failures (Noetzli and others, 2003; Gruber and others, 2004; Fischer and others, 2005) and the increased vulnerability of infrastructure and buildings in mountainous areas (Haeberli, 1992).

Various research endeavors aimed at providing a better understanding of mountain permafrost have recently been launched (e.g. the European Commission (EC)-funded Permafrost and Climate in Europe (PACE) project; Harris and others, 2003). It is now recognized that detailed knowledge of the internal structure of permafrost is required

for the optimum design of hazard-mitigation measures and for the numerical modeling of the dynamic behavior of permafrost (Arenson and others, 2002, Kääb and Weber, 2004). Diffusive electromagnetic, geoelectric, seismic and ground-penetrating radar (georadar) techniques have proven to be suitable tools for determining the internal structure of permafrost in many regions. However, the use of such geophysical techniques on rock glaciers is complicated by several factors:

1. Accessibility in high mountain areas and the pronounced topographic relief of rock glaciers may be the source of major logistical problems.
2. Electrical resistivities of crystalline rocks and ice can be extremely high, making it difficult to inject electric currents into the ground using galvanic methods.
3. Strong scattering of seismic and georadar waves within the highly heterogeneous mixtures of boulders, unconsolidated sediments, ice, water and large voids can obscure reflected signals.

All these factors make geophysical surveying on rock glaciers an extremely challenging task and require very careful planning of the experiments. It is our experience that the time required to perform a survey on a rock glacier is increased by a factor of 5–10 compared with a similar experiment in a more convenient environment.

Most geophysical case studies of mountain permafrost reported in the literature have involved applications of sounding methods that provide one-dimensional (1-D) distributions of physical properties as functions of depth and/or lateral mapping methods that supply information on

the horizontal variations of physical properties over a narrow depth range. Only recently have applications of two-dimensional (2-D) imaging (tomographic inversion) techniques to mountain permafrost been reported (e.g. Kneisel and others, 2000; Ishikawa and others, 2001; Musil and others, 2002; Hauck and others, 2003, 2004; Marescot and others, 2003; Heggem and others, 2005). These imaging techniques provide more reliable and more complete information than the sounding and lateral mapping methods.

In this contribution, we begin by reviewing state-of-the-art geophysical techniques that can be applied in investigations of alpine permafrost. We concentrate on the peculiarities that need to be considered in investigations of rock glaciers. We then present the results of two multi-parameter field studies conducted on a slow- and a fast-moving rock glacier in the eastern Swiss Alps. On the basis of our results, we propose a general template for geophysically investigating alpine permafrost.

2. GEOPHYSICAL 2-D IMAGING METHODS

2.1. Diffusive electromagnetic techniques

Diffusive electromagnetic techniques are mostly sensitive to electrical resistivity, which can vary by orders of magnitude for typical permafrost materials (Table 1). Since the electromagnetic coupling is inductive, the sources and receivers need not be in direct contact with the ground. Consequently, the techniques can be used for ground and airborne surveying (Hoekstra, 1978; Todd and Dallimore, 1998; Hauck and others, 2001, Bucki and others, 2004).

In practice, frequency-domain (FDEM) and time-domain (TDEM) electromagnetic systems are employed (e.g. Reynolds, 1997). Since the source–receiver separations of many FDEM systems need to be accurately known, rigidly mounted units (e.g. the EM-31; McNeill, 1980) are usually used for surveying rugged mountainous terrains. Alternatively, in areas where there is good radio reception, the versatile radiomagnetotelluric method may supply useful information (Beylich and others, 2003).

Typical TDEM systems require transmitter loops with diameters of a few meters to a few tens of meters. Deploying large loops across blocky rock glaciers can be quite laborious, and only a few measurements per day may be possible. As a consequence, TDEM systems are best suited for soundings under these conditions, because only a single layout needs to be set up per sounding. The generally resistive mountain permafrost poses further problems for TDEM data acquisition; since the secondary magnetic fields decay rapidly once the electric currents are turned off, TDEM recording systems need to densely sample the fields at early times.

During the past decade, 2-D and three-dimensional (3-D) tomographic inversion techniques for FDEM and TDEM data have been developed (e.g. Newman and Alumbaugh, 1997). Yet, to our knowledge, no tomographic inversion results from mountain permafrost have been reported in the literature. Reasons for this may include the time-consuming effort required to record spatially dense datasets, and the lack of commercially available inversion software. Two-dimensional resistivity cross-sections have been produced by interpolating the inversion results of several independent 1-D electromagnetic soundings (Todd and Dallimore, 1998; Bucki and others, 2004).

Table 1. Physical parameters that are relevant for geophysical surveying of rock glaciers

	Electrical resistivity $\Omega\text{ m}$	Seismic speed m s^{-1}	Georadar speed $\text{m } \mu\text{s}^{-1}$
Rock	$10^3\text{--}10^5$	3000–5500	80–150
Sand/gravel	$10^2\text{--}10^4$	500–2500	80–120
Ice	$10^6\text{--}10^7$	3500	170
Water	$10^1\text{--}10^2$	1500	30
Air	10^{14}	330	300

2.2. Goelectric techniques

Goelectric techniques can also be employed to determine the electrical resistivity of the ground. The lightweight equipment required to perform goelectric surveys can be transported to areas with difficult access. Application of tomographic inversion techniques to goelectric data requires a large number of measurements, which can be made efficiently with modern multichannel systems that include several tens of electrodes (e.g. Stummer and others, 2002). The most significant problem in goelectric surveying on rock glaciers is the weak galvanic coupling associated with the generally high contact resistances. To compensate for this, we attach water-soaked sponges to the electrodes, and water the immediate vicinity of the electrodes (Fig. 1a). Nevertheless, the currents injected into the ground and the measured voltages are generally low. This issue needs to be considered when selecting the electrode configuration to be used. Because electrode configurations with low geometrical factors provide larger voltages (e.g. Reynolds, 1997), Wenner configurations are generally more suitable for surveying rock glaciers than dipole–dipole configurations. Since snow cover may prohibit the current injection, we prefer to conduct our goelectric surveys in the summer.

Over the past two decades, tomographic inversion techniques for goelectric data have become increasingly popular and user-friendly (<http://www.abem.se/>). Application of these programs to mountain permafrost data poses no serious problems so long as they correctly account for the effects of the pronounced topographic relief.

2.3. Seismic techniques

Seismic techniques are mostly sensitive to elastic parameter variations that govern the propagation speed of compressional waves (P-waves). Characteristic P-wave speeds of mountain permafrost materials are quite different (Table 1). Applications of high-resolution seismic techniques require a relatively large number of closely spaced receiver and source positions. Typical deployments may include 48–120 geophones equally spaced at 1–5 m. Ideally, the density of sources should be comparable to that of the receivers. However, to minimize time in the field, the density of sources may be substantially less than this.

Surface conditions on rock glaciers make it difficult to couple the geophones and seismic sources to the ground. One option is to conduct seismic surveys during the winter. This alleviates the field effort significantly, but the snow cover may cause the seismic data to be highly contaminated with guided phases that obscure the reflections (Musil and others, 2002). Our preference is to conduct seismic surveys

during the summer. For uniformly good geophone–ground coupling, we fasten the geophones to the surface boulders by drilling small holes (Fig. 1b). The extremely heterogeneous near-surface environment causes substantial attenuation of the seismic waves. Such attenuating conditions usually preclude the use of low-energy sources (e.g. sledgehammers and pipeguns) and the difficult terrain precludes the use of mini-vibrators and weight-drop devices (Van der Veen and others, 2000). Explosives loaded into shallow boreholes drilled into the boulders or pushed into crevices between the boulders provide high levels of energy in a cost-effective manner. To record data over distances of 100–200 m, charge sizes of 100–500 g are necessary.

Near-surface attenuation results in the preferential loss of the high-frequency seismic signal. In combination with the presence of strong scattered energy and guided phases, this makes it extremely difficult to image reflections in rock glacier seismic data (Musil and others, 2002). By comparison, it is now quite straightforward to extract reliable information from the first-arriving direct and refracted phases. Although simple analysis techniques (e.g. the generalized reciprocal method; Palmer, 1980) can be employed for mapping first-order discontinuities underlying relatively uniform overburden, more sophisticated 2-D tomographic inversion techniques are required for analyzing rock glacier seismic data. The geophysical literature describes tomographic inversion algorithms based on two-point ray tracing (Zelt and Smith, 1992) and finite-difference Eikonal solvers (Lanz and others, 1998), the latter being the preferred choice for data distinguished by strong lateral speed variations.

2.4. Georadar surveying

The high electrical resistivity of most mountain permafrost terrains is a positive characteristic for georadar surveying. In such environments, the georadar techniques are most sensitive to variations in dielectric permittivity, which govern the propagation speeds of georadar waves. Characteristic georadar wave speeds in mountain permafrost materials vary significantly (Table 1).

The high resistivities allow antennas with dominant frequencies as low as 1 MHz to be employed (Gogenini and others, 1998). For high-resolution investigations, antennas with dominant frequencies between 20 and 100 MHz have proven to be suitable (Arcone and others, 1998; Isaksen and others, 2000; Lehmann and Green, 2000; Berthling and others, 2003; Moorman and others, 2003). Proper coupling of the antennas to the ground is an important prerequisite for recording high-quality data. This can be realized in winter, when the snow cover provides uniform surface conditions. A constant distance between the transmitter and receiver antennas is achieved by mounting both on a single sledge. Another critical concern in acquiring georadar data is accurate positioning. High-resolution investigations with measurement spacings of a few tens of centimeters require the use of automatic positioning systems (Lehmann and Green, 1999; Streich and others 2006).

Techniques adopted from seismic reflection data processing can be used to obtain detailed subsurface images from the recorded georadar data. Commonly employed processing steps include amplitude scaling to enhance later-arriving events relative to the earlier-arriving ones and frequency filtering in the time and space domains to remove system noise and improve the coherency of reflected signals

(Gross and others, 2003). If reliable speed information is available, migration may be used to convert the processed time sections to equivalent depth sections. To account for the effects of strong topographic relief, special-purpose topographic migration algorithms may be applied (Lehmann and Green, 2000; Heincke and others, 2005).

In small areas (e.g. $50 \times 50 \text{ m}^2$) of particular interest, 3-D georadar experiments can be performed. This technique has proven to be highly successful in various applications (Grasmueck and others, 2004; Gross and others, 2004; Heincke and others, 2005) and is expected to work well on mountain permafrost. To obtain unaliased subsurface images, it is critical that the investigation area be very densely sampled.

2.5. Cross-hole methods

Conceptually, most geophysical techniques can also be applied in a cross-hole mode (e.g. by placing the sources in one borehole and recording the data in another). Cross-hole tomography provides detailed 2-D information in the plane containing the two boreholes. The multiple illumination of subsurface targets provided by cross-hole geometries results in more reliable and higher-resolution information than can be provided by most surface-based techniques. Ideally, the borehole separation should be about half the borehole depth.

Unfortunately, boreholes in mountain permafrost usually provide less-than-ideal conditions for geophysical experiments (Arenson and others, 2002). The general absence of water and the presence of casing to stabilize the boreholes may substantially complicate applications of certain geophysical techniques. Diffusive electromagnetic and radar systems can see through PVC casing, but not through metal casing. For geoelectric surveys, borehole electrodes that can be operated in dry uncased holes require centralizers with metal clamping arms. In the presence of casing, the electrodes need to be attached to the outside of the casing before it is inserted into the borehole. To compensate for the absence of water, instead of using standard piezoelectric sources and receivers (i.e. hydrophones) for borehole seismic experiments, more complicated seismic sources and receivers (i.e. geophones) need to be clamped to the borehole casing or walls.

3. MURTÈL CASE STUDY

3.1. Site description

The Murtèl rock glacier is located in the Upper Engadine area of the eastern Swiss Alps. It is ~ 150 m wide, 300 m long and extends over an altitude range of 2600–2800 m (Fig. 2). It is moving horizontally a few centimeters per year (Kääb and Weber, 2004). The ongoing movements have generated numerous flow lobes (Fig. 2). In 1987, a borehole was drilled to 58 m depth (Vonder Mühl and Holub, 1992). It encountered, at successively greater depths: large boulders and air-filled voids at 0–3 m; an ice-rich layer (more than 40% ice) at 3–15 m; a mixture of ice and sand (30–35% ice) at 15–30 m; and a mixture of sands and boulders at 30–52 m, and bedrock below.

In an attempt to determine the internal structure of the Murtèl rock glacier, we recorded TDEM data and acquired surface-based geoelectric, seismic tomographic and georadar data along nearly coincident lines parallel to the rock glacier flow direction (Fig. 2). Here, we focus on the integration of information provided by the four datasets.

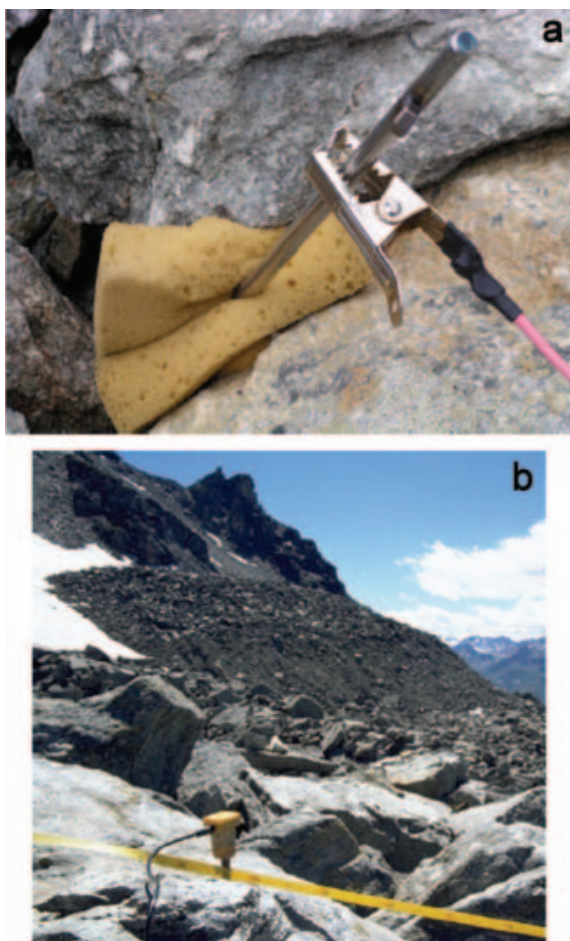


Fig. 1. (a) Galvanic coupling of an electrode in the blocky environment of a rock glacier. (b) Geophone fastened to a boulder of a rock glacier using a small drillhole (yellow stripe at the bottom of the image is a measuring tape).

3.2. TDEM survey

TDEM data provided first-order estimates of rock glacier thickness (Hauck and others, 2001). In principle, this type of information could be obtained directly from the borehole logs, but to investigate the suitability of the TDEM method on rock glaciers, a sounding was performed near the borehole (Hauck and others, 2001). Acquisition time was about half an hour. The TDEM data were inverted using TEMIX, a commercial software package (Interpex Limited, 1990).

Results of the TDEM survey are depicted in Figure 3. Figure 3a shows the observed data plotted as apparent resistivity vs time since current turn-off. From the general shape of this curve, we can infer the presence of a relatively resistive layer sandwiched between two more conductive layers, one of which approaches the surface. The solid line in Figure 3b represents the best-fitting model obtained from the inversion program, and the gray shaded area represents 'equivalent' models that explain the data nearly as well as the best-fitting model (Nabighian and Macnae, 1987). The significant decrease of resistivity at 54 ± 15 m depth coincides with the rock-glacier–bedrock interface.

3.3. Tomographic geoelectric survey

We made 103 Wenner geoelectric measurements along a 145 m long profile across the frontal region of the rock

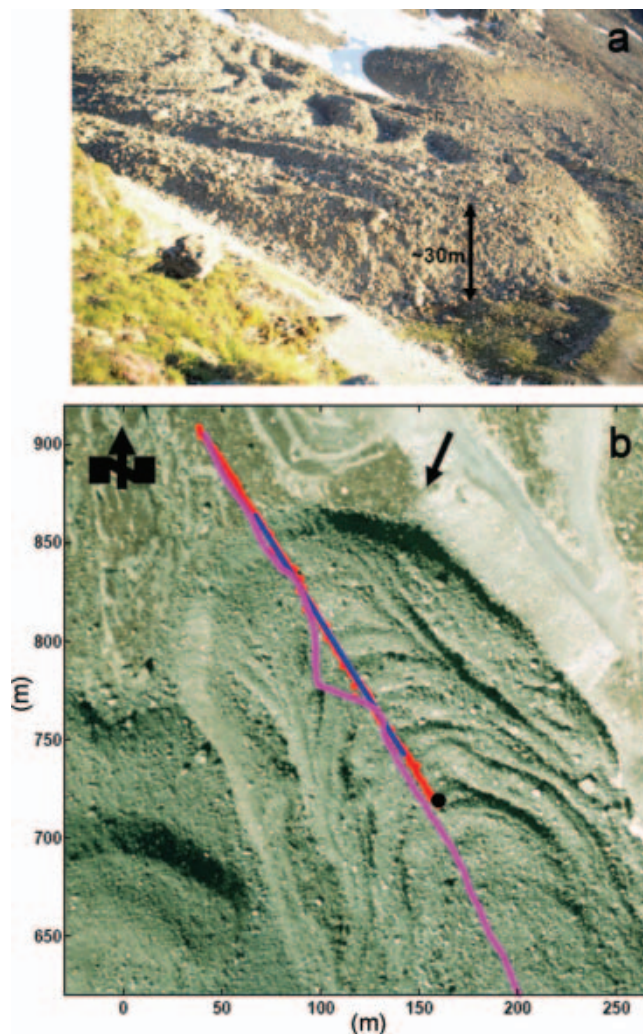


Fig. 2. (a) Photograph of the Murtèl rock glacier. View direction is indicated with a black arrow in (b). (b) Orthophoto of the Murtèl rock glacier showing the locations of the borehole (black dot) and the geoelectric (blue), seismic (red) and georadar (magenta) profiles.

glacier (Fig. 2), deploying 30 electrodes equally spaced at 5 m intervals. Electrode coupling was especially difficult on this rock glacier, because the surface consisted of large boulders (up to 2 m high) with only small amounts of fine-grained material. The total acquisition time was 5 hours. Our geoelectric data were tomographically inverted using RES2DINV, a commercial software package (<http://www.abem.se/>).

A moderately conductive near-surface layer (DC1) with a resistivity of ~ 10 k Ω m and a thickness of about ± 2.5 m is observed along the length of the recording line (Fig. 4a; DC1 in Fig. 4c). Within the rock glacier, i.e. below DC1, in the horizontal distance range 50–140 m, the resistivity increases abruptly to the M Ω m range. At about 140 m horizontal distance, near where the surface exposure of the rock glacier ends, resistivities at depth change from the M Ω m range to the k Ω m range across a steeply dipping boundary denoted as DC2 in Figure 4c.

3.4. Tomographic seismic survey

Our tomographic seismic experiment across the Murtèl rock glacier was conducted during the summer. Using a 120-channel seismograph, 120 geophones spaced at 2 m intervals

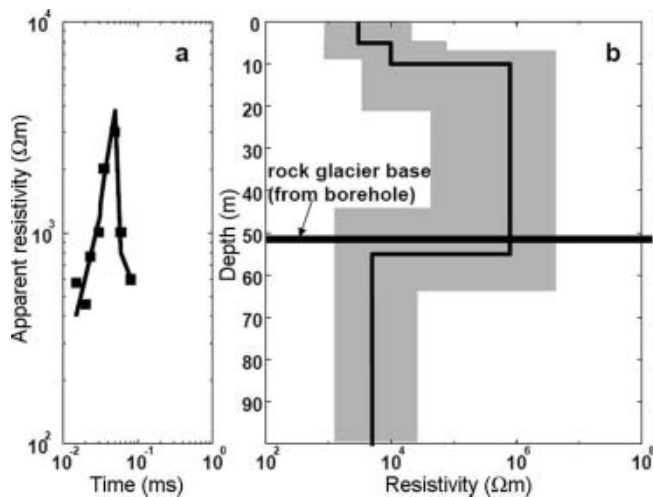


Fig. 3. Results of a TDEM sounding on the Murtèl rock glacier. (a) The observed (squares) and predicted (solid line) data based on the best-fitting model shown by the solid line in (b). Gray shaded area in (b) indicates the range of equivalent models that explain the data nearly as well as the best-fitting model.

and 44 sources (charges of 200–400 g) spaced at ~ 5.4 m intervals, we acquired data along a 238 m long profile. Four days were required to record the data. Data inversion was performed using the tomographic program described by Lanz and others (1998).

The resulting speed tomogram contains three principal units (Fig. 4b and d). A laterally extensive surface layer, S1, with speeds < 2000 m s^{-1} (Fig. 4d) is underlain in most regions by material with intermediate speeds of 3000–4000 m s^{-1} . In the deepest regions of the tomogram, the speeds are > 4000 m s^{-1} . The interface between the middle and lower units is labeled S2 in Figure 4d. At a horizontal distance of ~ 90 m, an isolated high-speed feature is observed immediately below the low-speed surface layer (S3 in Fig. 4d). Although the spatial extent of S3 is quite small, it appeared in all our inversion runs using different initial models and regularization parameters. The frontal part of the rock glacier exhibits pronounced speed contrasts, with a 10–15 m thick surface block of very low-speed material overlying rocks with speeds > 5000 m s^{-1} .

3.5. Georadar survey

We used 50 MHz antennas and a station spacing of 0.5 m to record georadar data along a ~ 350 m long profile (Fig. 2b). A relatively simple processing scheme that included automatic gain control, frequency filtering, spectral whitening and F-X deconvolution was applied to the data. Unfortunately, no detailed speed information was available along the profile, which precluded us from applying topographic migration. Instead, we performed a simple time-to-depth conversion using a speed of 120 $\text{m } \mu\text{s}^{-1}$ (based on a common-midpoint measurement in the central part of the rock glacier). Appraisal of a depth error associated with the overly simplified assumption of a homogeneous speed is difficult, but we judge that depth errors should not exceed 10%. The final section is displayed in Figure 5. Maximum depth penetration of the georadar signals is about 50 m. Several prominent dipping reflections extend over substantial portions of the profile (highlighted by black lines in Fig. 5b).

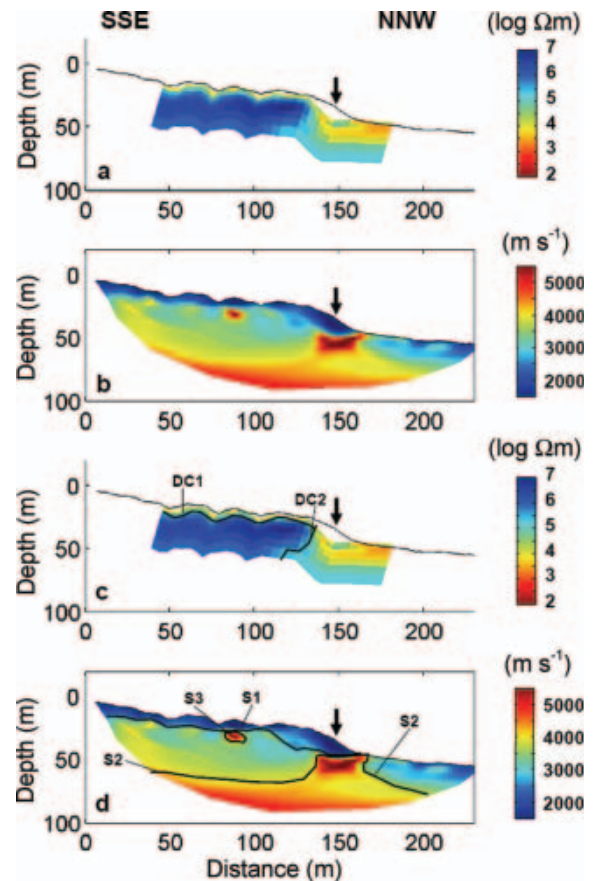


Fig. 4. (a, b) Results from the (a) geoelectric and (b) seismic surveys conducted on the Murtèl rock glacier. (c, d) Our interpretations superimposed on the tomograms of (a) and (b) respectively. Topography defined by the coordinates of the geophones is superimposed on all sections. Location of the profile is shown in Figure 2. Frontal part of the rock glacier is marked in all panels with a black arrow. DC1 and S1 denote the active layer, DC2 is the boundary between frozen and unfrozen material, S2 is the bedrock interface and S3 is probably a huge boulder.

3.6. Integrated interpretation

Figure 6 shows a sketch of our interpretation of important features identified in the geoelectric, seismic and georadar images. Our interpretation is constrained by information provided by the borehole. The nearly coincident DC1 and S1 layers represent the bottom of the active layer, which melts in the summer and freezes in the winter. This active layer, which corresponds to loose boulders at the top of the borehole, has moderate resistivities of ~ 10 $\text{k}\Omega\text{m}$ and low seismic speeds of < 2000 m s^{-1} . The resolution capabilities of TDEM soundings in the uppermost 10 m are limited and should always be interpreted cautiously (e.g. Nabighian and Macnae, 1991). Nevertheless, it is interesting to note that the near-surface 10 $\text{k}\Omega\text{m}$ values shown in Figure 3 are consistent with our interpretation.

The very high resistivities in Figure 4a and c are evidence for high ice content within the core of the rock glacier. This is consistent with the borehole log. A sharp lateral change to lower resistivities at DC2 delineates the beginning of unfrozen material at the front of the rock glacier, and the isolated high-speed body, S3, probably represents a large boulder (Fig. 4d) not represented in the other geophysical datasets.

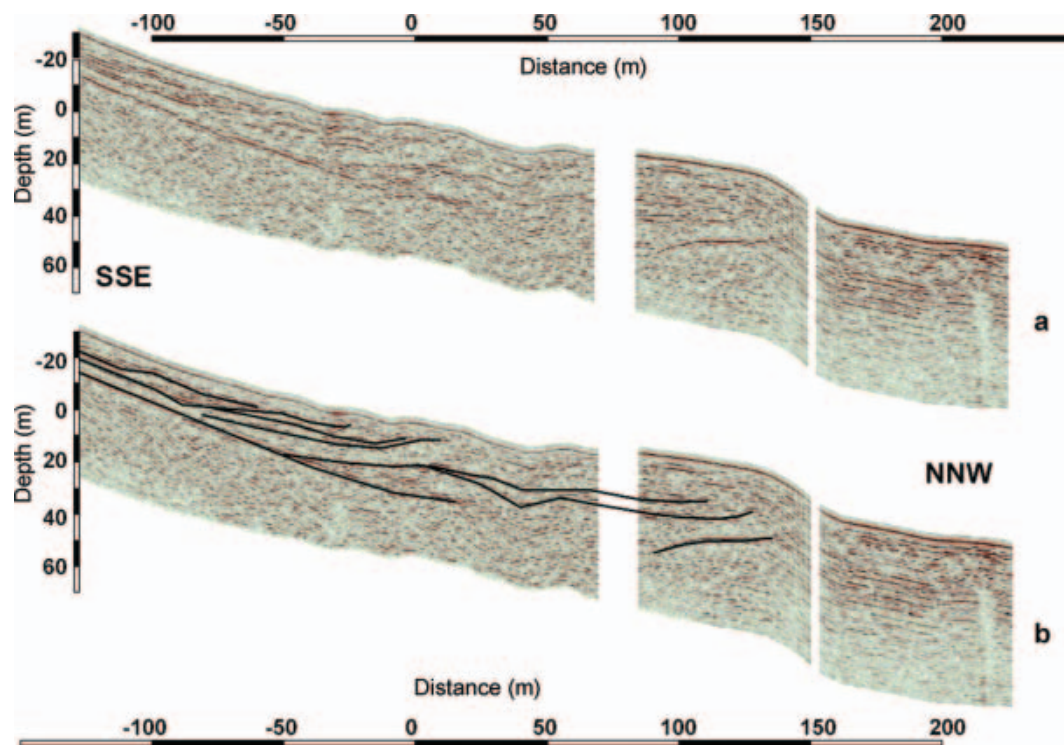


Fig. 5. (a) Georadar section recorded along the Murtèl rock glacier. (b) Our interpretation superimposed on the georadar section. Location of the profile is shown in Figure 2.

The series of reflections observed in the up-glacier part of the georadar section (Fig. 5) are most likely to originate from alternating snow and debris accumulations created by mass movement events from the slope above the rock glacier. Such features are quite common in georadar images of the upper part of rock glaciers; they represent the snow and debris sources that define the typical morphology of rock glacier bodies (e.g. Berthling and others, 2003). In the central and down-glacier parts of the georadar section, the two dominant reflections originate from the ice-rich and moderately ice-rich layers observed in the borehole (reflection intersects the borehole at the boundary between ice-rich and sand and ice layers; Fig. 6). The deeper reflection at $\sim 20\text{--}30\text{ m}$ depth between 0 and 125 m distance corresponds to the bottom of the ice-containing units and to the shear horizon observed in the inclinometer measurements described by Vonder Mühl and Holub (1992). Their measurements indicate displacement rates of 0.04 m a^{-1} at this depth.

The seismic speed discontinuity, S2, in Figure 4d defines the top of the bedrock. Towards the frontal part of the rock glacier, S2 becomes shallower, reaching the surface at about 170 m horizontal distance. The high bedrock speeds within this bedrock protrusion may indicate the presence of virtually unfractured rock that may have acted as a barrier to the flow of the rock glacier.

4. MURAGL CASE STUDY

4.1. Site description

The Muragl rock glacier is also located in the Upper Engadine area. It is 100–300 m wide, $\sim 700\text{ m}$ long and extends over an altitude range of 2600–2800 m (Fig. 7). It is distinguished by rapid horizontal movements of up to

0.5 m a^{-1} (Kääb and Vollmer, 2000). This is substantially faster than typical rock glacier movements, which are of the order of several cm a^{-1} . Like the Murtèl rock glacier, it exhibits pronounced flow lobes with transverse furrows and ridges. The irregular flow-lobe pattern of the Muragl rock glacier (compare Fig. 7b with Fig. 2b) may be the result of periodic mass movements, perhaps reflecting several generations of rock glacier evolution. In 1999, four boreholes, B1–B4, were drilled through the rock glacier to bedrock

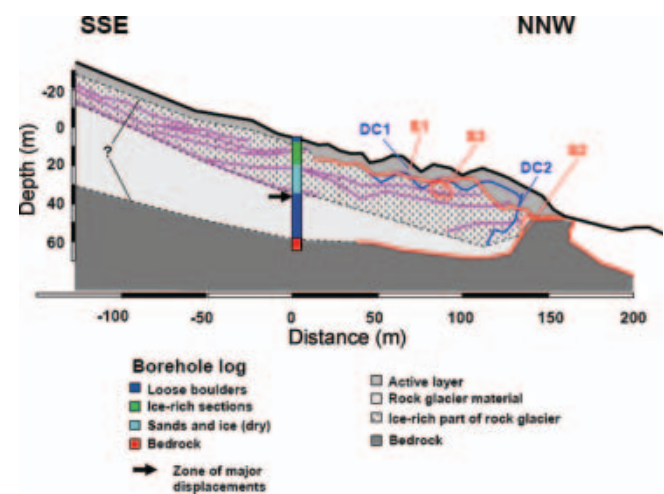


Fig. 6. Integrated interpretation of boundaries observed in the geoelectric (blue lines), seismic (red lines) and georadar (magenta lines) images from the Murtèl rock glacier. The borehole log is also displayed. DC1 and S1 denote the active layer, DC2 is the boundary between frozen and unfrozen material, S2 is the bedrock interface and S3 is probably a huge boulder.

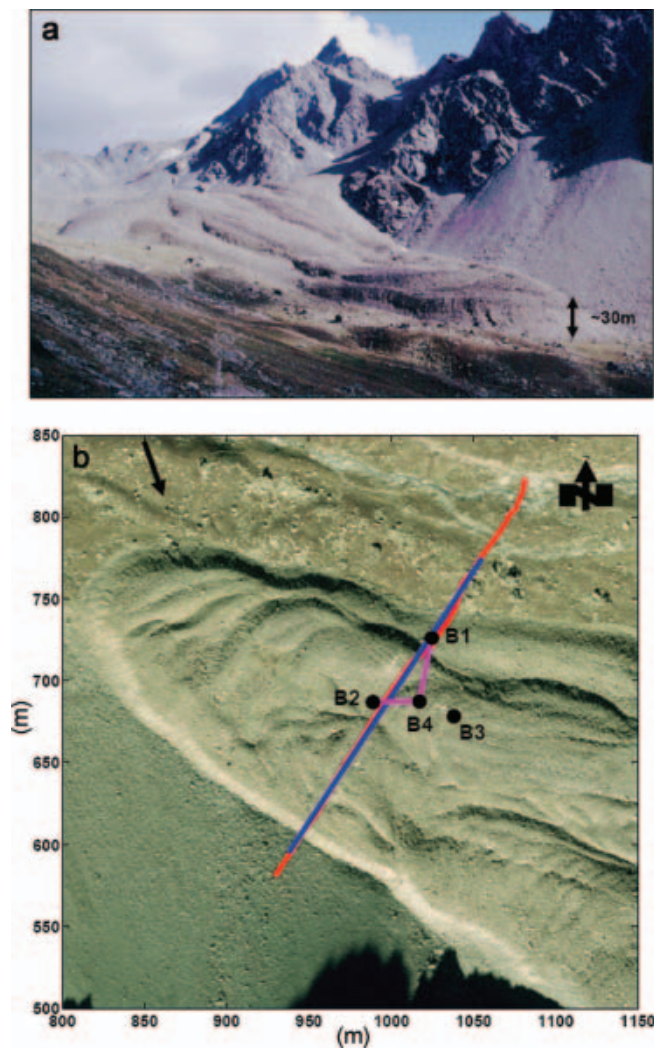


Fig. 7. (a) Photograph of the Muragl rock glacier. View direction is indicated with a black arrow in (b). (b) Orthophoto of the Muragl rock glacier showing the locations of the boreholes (black dots), the surface geoelectric (blue) and seismic (red) profiles and the cross-hole georadar (magenta) sections.

(Arenson and others, 2002; Fig. 7b). A more detailed description of the borehole logs is deferred to section 4.5, but the geology at progressively greater depths can be described as: (i) loose boulders, (ii) a mixture of sand, boulders and ice, (iii) a zone of boulders and voids, (iv) sand that is mostly free of ice and (v) bedrock at 32–45 m depth. Thin water-saturated zones are found within the core of the rock glacier.

One goal of our project was to compare the internal structures of the slow-moving Murtèl and fast-moving Muragl rock glaciers. Accordingly, we attempted to collect similar datasets at the two study sites. Unfortunately, the surface-based georadar and TDEM sounding data collected across the Muragl rock glacier did not yield useful information, possibly as a result of scattering and absorption of the electromagnetic energy within a more complex rock glacier mass. In contrast, the surface geoelectric and seismic surveys and the cross-hole radar experiments produced many useful data. For logistic reasons, we could only collect data along the axis of the Murtèl rock glacier (Fig. 2b) and along a direction perpendicular to the axis of the Muragl rock glacier (Fig. 7b).

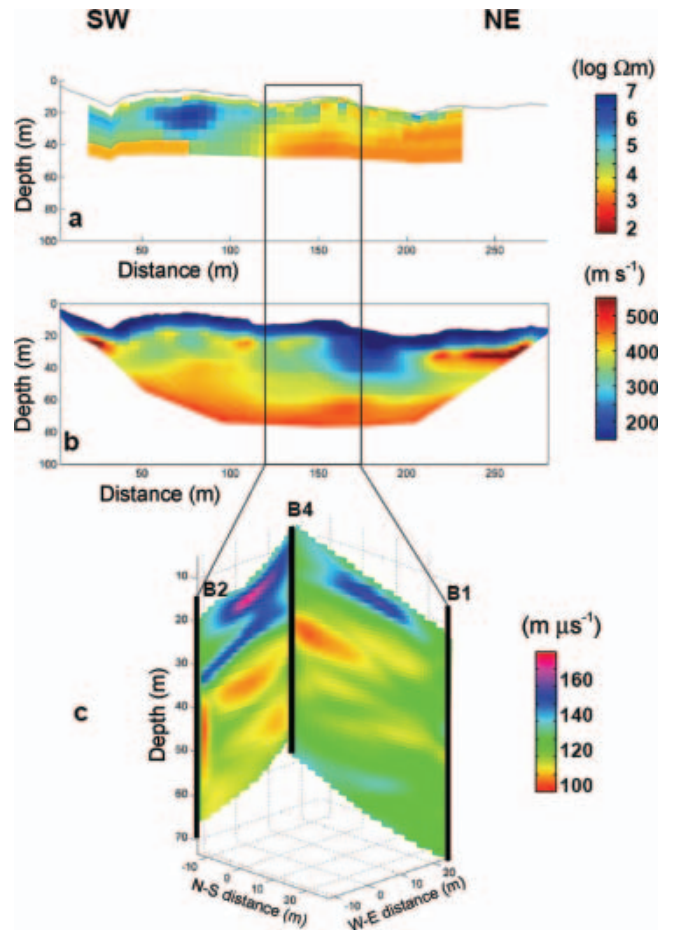


Fig. 8. Results from the (a) geoelectric, (b) seismic and (c) cross-hole georadar surveys conducted on the Muragl rock glacier. Topography defined by the coordinates of the geophones is superimposed on (a) and (b). Note that geoelectric data were acquired in summer and seismic data were recorded in winter. Differences in topography are caused by the snow cover during the seismic campaign. Locations of the surveys are shown in Figure 7.

4.2. Tomographic geoelectric survey

We employed very similar recording parameters and identical data inversion software for the Murtèl and Muragl rock glacier investigations. The resultant uninterpreted and interpreted resistivity tomograms for the Muragl rock glacier are shown in Figures 8a and 9a, respectively.

A thin layer of moderately high-resistivity material underlies the undulating surface (DC1 in Fig. 9a). This is underlain in the southwest part of the survey line by higher-resistivity material (several tens of kΩm; DC2 in Fig. 9a). Within DC2, there is a highly resistive core with resistivities in the MΩm range (DC3 in Fig. 9a). The remaining regions of the tomogram have resistivities of several kΩm.

4.3. Tomographic seismic survey

In contrast to the Murtèl field campaign, we acquired our seismic data across the Muragl rock glacier during the winter. Geophones were planted in a compacted layer of surface snow, and the dynamite charges were placed 1–2 m beneath the surface at the base of the snow layer. Technical details of the seismic data acquisition and processing are given by Musil and others (2002). We again used a 120-channel seismograph, but the 120 geophones were spaced at 2.5 m

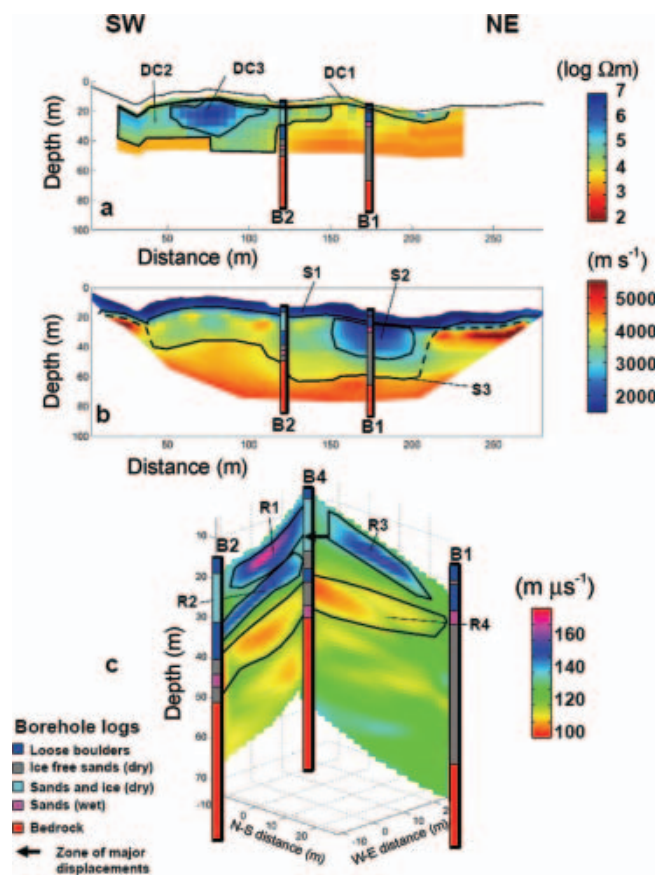


Fig. 9. As for Figure 8, but with our interpretations superimposed on the tomograms. The borehole logs are also displayed. DC1 and S1 represent the active layer, DC3 is the ice-rich core of the rock glacier, S2 represents degraded permafrost and S3 is the bedrock interface. R1 represents an ice-rich zone, R2 is a layer with large voids, R3 is either ice-rich or includes voids (see text) and R4 is the water-saturated part of the rock glacier.

intervals and the 53 sources were separated from each other by ~ 5.6 m. The total profile length was 297.5 m (Fig. 7).

The resultant tomographic seismic image in Figure 8b is characterized by pronounced variations of seismic speed. A 5–10 m thick surface layer of low-speed material extends the length of the line (S1 in Fig. 9b). Between 160 and 200 m horizontal distance, low speeds can be traced to even greater depths (low-speed body S2 in Fig. 9b). Towards both ends of the profile, speeds immediately below the near-surface low-speed layer are >4000 m s^{-1} . Speeds are uniformly >4000 m s^{-1} along the base of the entire image (interface S3 in Fig. 9b delineates approximately the upper boundary of speeds >4000 m s^{-1}).

4.4. Cross-hole radar survey

Using low-frequency (22 MHz) transmitter and receiver antennas (~ 3 m long), cross-hole radar data were collected between boreholes B4 and B1 and between B4 and B2. Transmitter and receiver spacings were both 1 m. Tomographic inversions of the travel-time data were performed using an algorithm described by Maurer and Green (1997). Further details of the experiment can be found in Musil and others (2006).

Perspective images of the tomographic planes B4–B1 and B4–B2 are shown in Figures 8c and 9c. They are characterized by a background speed of ~ 120 $\text{m } \mu\text{s}^{-1}$ and

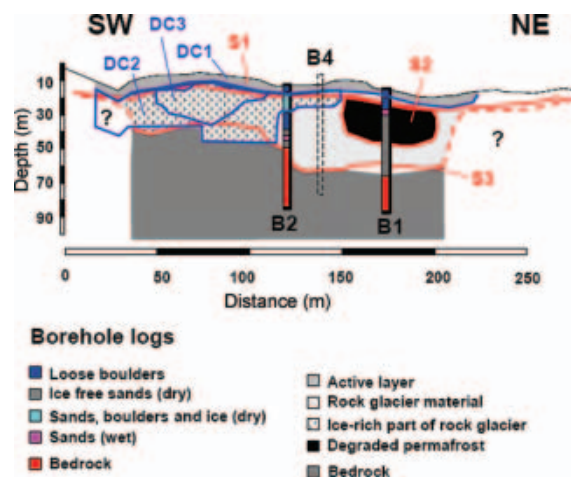


Fig. 10. Integrated interpretation of geoelectric (blue lines) and seismic (red lines) images from the Muragl rock glacier. The borehole logs of B1 and B2 are also displayed. DC1 and S1 represent the active layer, DC3 is the ice-rich core of the rock glacier, S2 represents degraded permafrost and S3 is the bedrock interface.

imbedded zones of both higher and lower speed. At depths of <35 m, there are three zones of distinctly higher speed with values reaching 160 $\text{m } \mu\text{s}^{-1}$ (R1, R2 and R3 in Fig. 9c), whereas in the depth interval 35–45 m the speeds are as low as 100 $\text{m } \mu\text{s}^{-1}$ (zone R4 in Fig. 9c).

4.5. Integrated interpretation

Figure 10 shows our interpretation of important features identified in the surface geoelectric and seismic and cross-hole georadar images. Again, our interpretation is strongly constrained by borehole information. The active layer is delineated by the geoelectric and seismic layers DC1 and S1 (Fig. 9). Since snow covered the ground during the seismic survey, S1 overestimates the thickness of the active layer.

The presence of ice is identified in the southwest part of the rock glacier by a combination of high resistivities and seismic speeds of about 3500 m s^{-1} (region DC2 in Figs 9a and 10). The resistivities are generally lower than those observed within the Murtèl rock glacier, perhaps indicating a higher proportion of unfrozen water and related warmer temperatures. Resistivities in the $\text{M } \Omega\text{m}$ range are only detected within the relatively small region, DC3. Although it is difficult to compare results from the longitudinal Murtèl profile with the perpendicular Muragl profile, based on the distributions of resistivity in Figures 4c and 9a it seems likely that the distribution of ice in the Muragl rock glacier is rather more heterogeneous than in the Murtèl rock glacier.

The low-seismic-speed block, S2, is distinguished by moderate resistivities, which according to borehole log B1 is due to the presence of voids filled with air (low seismic speed) and minor occurrences of water (decreased resistivities) (Fig. 10). Results from surface displacement analyses (Kääb and Vollmer, 2000) indicate that movements have practically ceased within this region. Taken together, these observations indicate that the permafrost has degraded in this part of the rock glacier (i.e. the ice has melted, leaving behind large voids).

Bedrock topography is defined primarily by the borehole logs and the seismic interface, S3, the approximate upper limit of 4000 m s^{-1} material. The minor discrepancy between the log and S3 at borehole B1 (Fig. 10) is probably due to

Table 2. Summary of key results from the investigations performed on the Murtèl and Muragl rock glaciers (n.a. = not applied, n.s. = not successful)

Rock glacier	TDEM	Geoelectrics	Seismic refraction tomography	Surface georadar	Borehole georadar
Murtèl	Approximate bedrock depth	Active layer, ice content, structure of frontal part	Active layer, large blocks, bedrock depth	Detailed internal structure of rock glacier	n.a.
Muragl	n.s.	Active layer, ice content, partially bedrock depth	Active layer, degraded permafrost, bedrock depth	n.s.	Ice-rich zones, voids, water content

3-D effects, with the seismic energy having traveled out-of-the-plane of the profile along a slightly shallower region of bedrock. The correlation between the lower boundary of the high-resistivity region DC2 and S3 varies from good at horizontal distances 40–70 m to poor at shorter and longer distances. Based on the air photograph in Figure 7b, we judge that S3 represents reasonably well the depth to bedrock beneath the southwest end of the line.

Radar features R1–R4 are not included in Figure 10, because the cross-hole tomographic planes are highly oblique to the plane containing the geoelectric and seismic tomograms (Fig. 7b). Nevertheless, a comparison of Figures 9c and 10 reveals some interesting correlations. For example, the high-speed zone, R1, coincides with the northeast lobe of the high-resistivity region, DC2, in which the pores between the sediments and boulders are filled with ice (see the ice-rich zones in the B2 and B4 borehole logs; Fig. 9c), whereas the underlying high-speed zone, R2, is located in a lower-resistivity region in which the pores are mostly empty (see the loose boulders and dry ice-free sands at the appropriate depths in the B2 and B4 borehole logs; Fig. 9c). These observations are entirely consistent with the relatively high radar speeds of ice ($170 \text{ m } \mu\text{s}^{-1}$) and air ($300 \text{ m } \mu\text{s}^{-1}$) and with the joint interpretations of georadar travel times and amplitudes of Musil and others (2006). To generate the high speeds observed in R2, the air voids must be quite large. Since it is not possible to maintain such voids in an active rock glacier over long periods, they were probably filled with ice until quite recently (Musil and others, 2006).

Interpretation of the high-speed zone, R3, is not conclusive. It could represent a zone with pores filled with ice or air. Since R3 extends close to borehole B1, which is situated within degraded permafrost, we prefer the option of air-filled voids. Finally, the low speeds of zone R4 may be associated with one or more water-bearing layers intersected in boreholes B1, B2 and B4 (Musil and others, 2006). There is no perfect correlation between the borehole logs and the tomograms. This may be the result of alterations caused by the drilling process.

Comparisons of the radar tomographic images with the results of inclinometer measurements performed in borehole B4 (Arenson and others, 2002) reveal an interesting similarity with the Murtèl rock glacier. As indicated by the black arrow in Figure 9c, most of the displacements are concentrated at the bottom of the ice-rich layer defined by the high-speed zone, R1. The much higher displacement rates at the Muragl rock glacier relative to those at the Murtèl rock glacier may be the result of generally higher temperatures close to the melting point of ice, as measured in the boreholes (Vonder Mühll and others, 2005).

5. CONCLUSIONS AND OUTLOOK

Our investigations of two alpine rock glaciers have demonstrated some of the possibilities and some of the limitations of applying high-resolution geophysical techniques in such environments. We have shown that it is generally feasible to obtain meaningful 2-D subsurface images, despite the extremely challenging data acquisition conditions. Several newly mapped features provide fresh insights into the stability, kinematics and dynamics of the rock glaciers (Table 2). Key results include the:

- locations and geometries of the active layers and bedrock surface,
- characterization of the Murtèl rock glacier frontal zone,
- spatial distributions of ice-, water- and air-filled voids in the Muragl rock glacier,
- delineation of internal structures such as shear zones.

Another important conclusion of our studies is that geoelectric, seismic and georadar data provide both redundant and complementary information. For example, ice-rich zones are best delineated on the basis of their very high electrical resistivities, whereas interfaces between loose and more compacted material (e.g. the base of the active layer, regions of degraded permafrost, the top of the bedrock) are best seen in seismic images. Surface-based georadar was the only method that allowed shear horizons to be determined, and borehole radar tomography revealed the presence of small-scale structures that were essentially invisible to the surface-based techniques.

For future investigations of rock glaciers or other mountainous regions underlain by permafrost we suggest the following template:

1. Use the fast and inexpensive (i) TDEM method to provide initial information on the gross (1-D) internal structures of the rock glaciers and their surroundings and (ii) surface-based georadar method to obtain detailed 2-D images of the same features.
2. On the basis of the TDEM soundings and georadar images, select appropriate locations and electrode spacings for acquiring multi-electrode geoelectric data along one or more profiles. Very-high-resistivity regions of the resultant electrical resistivity tomogram may delineate the spatial distribution of ice.
3. Depending on the available funds and the level of information required, it may be useful to collect seismic data. If bedrock topography is the target of primary interest, seismic data are essential. The geoelectric,

seismic and georadar data should be recorded along common profiles.

4. Based on the knowledge acquired as a result of steps 1–3, one or more boreholes should be drilled to ground-truth and/or calibrate the geophysical tomograms.
5. Considering the high costs of drilling, it is almost always worthwhile to record cross-hole and/or borehole-to-surface datasets. Choice of the data type (i.e. diffusive electromagnetic, geoelectric, seismic or georadar) depends on the problem.
6. In areas of particular interest (identified from the results of applying steps 1–5), small-scale 3-D georadar experiments may be performed.

ACKNOWLEDGEMENTS

This project would not have been feasible without the involvement of many people. We thank M. Musil, L. Arenson, S. Springman, D. Vonder Mühll, C. Kneisel, C. Baerlocher, M. Sperl, A. Seward, S. Metzger, H. Horstmeyer, T. Richter and the numerous field helpers for all their contributions. Financial support was provided by ETH Zürich (grant No. 0-20535), the EC project PACE and Academia Engadina. We thank A. Green for discussions and his thorough in-house review of the manuscript, which improved the quality of the paper substantially. Finally we acknowledge the helpful comments of reviewer B. Kulesa and an anonymous reviewer.

REFERENCES

- Arcone, S.A., D.E. Lawson, A.J. Delaney, J.C. Strasser and J.D. Strasser. 1998. Ground-penetrating radar reflection profiling of groundwater and bedrock in an area of discontinuous permafrost. *Geophysics*, **63**(5), 1573–1584.
- Arenson, L., M. Hoelzle and S. Springman. 2002. Borehole deformation measurements and internal structure of some rock glaciers in Switzerland. *Permafrost Periglac. Process*, **13**(2), 117–135.
- Berthling, I., B. Etzelmüller, M. Wåle and J.L. Sollid. 2003. Use of Ground Penetration Radar (GPR) soundings for investigating internal structures in rock glaciers. Examples from Prins Karls Forland, Svalbard. *Z. Geomorphol., Supplementband* 132, 103–121.
- Beylich, A.A. and 6 others. 2003. Assessment of chemical denudation rates using hydrological measurements, water chemistry analysis and electromagnetic geophysical data. *Permafrost Periglac. Process*, **14**(4), 387–397.
- Bucki, A.K., K.A. Echelmeyer and S. MacInnes. 2004. The thickness and internal structure of Fireweed rock glacier, Alaska, USA as determined by geophysical methods. *J. Glaciol.*, **50**(168), 67–75.
- Davies, M.C.R., O. Hamza and C. Harris. 2001. The effect of rise in mean annual air temperature on the stability of rock slopes containing ice-filled discontinuities. *Permafrost Periglac. Process*, **12**(1), 137–144.
- Fischer, L., A. Kääh, C. Huggel and J. Nötzli. 2005. Geology, glacier changes, permafrost and related slope instabilities in a high-mountain rock face: Monte Rosa east face, Italian Alps. *Geophys. Res. Abstr.*, **7**, 00518.
- Gogineni, S., T. Chuah, C. Allen, K. Jezek and R.K. Moore. 1998. An improved coherent radar depth sounder. *J. Glaciol.*, **44**(148), 659–669.
- Grasmueck, M., R. Weger and H. Horstmeyer. 2004. Three-dimensional ground-penetrating radar imaging of sedimentary structures, fractures, and archaeological features at submeter resolution. *Geology*, **32**(11), 933–936.
- Gross, R., A. Green, H. Horstmeyer, K. Holliger and J. Baldwin. 2003. 3-D georadar images of an active fault: efficient data acquisition, processing and interpretation strategies. *Subsurf. Sens. Technol. Appl.*, **4**(1), 19–40.
- Gross, R., A.G. Green, H. Horstmeyer and J.H. Begg. 2004. Location and geometry of the Wellington Fault (New Zealand) defined by detailed three-dimensional georadar data. *J. Geophys. Res.*, **109**(B5), B05401. (10.1029/2003JB002615.)
- Gruber, S., M. Hoelzle and W. Haeblerli. 2004. Permafrost thaw and destabilization of Alpine rock walls in the hot summer of 2003. *Geophys. Res. Lett.*, **31**(13), L13504. (10.1029/2004GL020051.)
- Haeblerli, W. 1992. Construction, environmental problems and natural hazards in periglacial mountain belts. *Permafrost Periglac. Process*, **3**(2), 111–124.
- Harris, C. and 9 others. 2003. Warming permafrost in European mountains. *Global Planet. Change*, **39**(3–4), 215–225.
- Hauck, C. and D. Vonder Mühll. 2003. Using DC resistivity tomography to detect and characterise mountain permafrost. *Geophys. Prospect.*, **51**(4), 273–284.
- Hauck, C., M. Guglielmin, K. Isaksen and D. Vonder Mühll. 2001. Applicability of frequency domain and time-domain electromagnetic methods. *Permafrost Periglac. Process*, **12**(1), 39–52.
- Hauck, C., K. Isaksen, D.S. Vonder Mühll and J.L. Sollid. 2004. Geophysical surveys designed to delineate the altitudinal limit of mountain permafrost: an example from Jotunheimen, Norway. *Permafrost Periglac. Process*, **15**(3), 191–205.
- Heggem, E.S.F., H. Juliussen and B. Etzelmüller. 2005. Mountain permafrost in Central-Eastern Norway. *Nor. Geogr. Tidsskr.* **59**(2), 94–108.
- Heincke, B., A.G. Green, J. van der Kruk and H. Horstmeyer. 2005. Acquisition and processing strategies for 3D georadar surveying a region characterized by rugged topography. *Geophysics*, **70**(6), K53–K61.
- Hoekstra, P. 1978. Electromagnetic methods for mapping shallow permafrost. *Geophysics*, **43**(4), 782–787.
- Interpex Limited. 1990. *TEMIX user's manual*. Golden, CO, Interpex Limited.
- Isaksen, K., R.S. Ödegård, T. Eiken and J.L. Sollid. 2000. Composition, flow and development of two tongue-shaped rock glaciers in the permafrost of Svalbard. *Permafrost Periglac. Process*, **11**(3), 241–257.
- Ishikawa, M., T. Watanabe and N. Nakamura. 2001. Genetic difference of rock glaciers and the discontinuous mountain permafrost zone in Kanchanjunga Himal, Eastern Nepal. *Permafrost Periglac. Process*, **12**(3), 243–253.
- Kääh, A. and M. Vollmer. 2000. Surface geometry, thickness changes and flow fields on permafrost streams: automatic extraction by digital image analysis. *Permafrost Periglac. Process*, **11**(4), 315–326.
- Kääh, A. and M. Weber. 2004. Development of transverse ridges on rock glaciers: field measurements and laboratory experiments. *Permafrost Periglac. Proc.*, **15**, 379–391.
- Kneisel, C. 2004. New insights into mountain permafrost occurrence and characteristics in glacier forefields at high altitude through the application of 2D resistivity imaging. *Permafrost Periglac. Process*, **15**(3), 221–227.
- Kneisel, C., C. Hauck and D.S. Vonder Mühll. 2000. Permafrost below the timberline confirmed and characterized by geoelectrical resistivity measurements, Bever Valley, eastern Swiss Alps. *Permafrost Periglac. Process*, **11**, 295–304.
- Lanz, E., H.R. Maurer, A.G. Green and J. Ansorge. 1998. Refraction tomography over a buried waste disposal site. *Geophysics*, **63**(4), 1414–1433.
- Lehmann, F. and A.G. Green. 1999. Semi-automated georadar acquisition in three dimensions. *Geophysics*, **64**, 719–731.
- Lehmann, F. and A.G. Green. 2000. Topographic migration of georadar data: implications for acquisition and processing. *Geophysics*, **65**(3), 836–848.

- Marescot, L., M.H. Loke, D. Chapellier, R. Delaloye, C. Lambiel and E. Reynard. 2003. Assessing reliability of 2D resistivity imaging in permafrost and rock glaciers using the depth of investigation index method. *Near Surf. Geophys.*, **1**(2), 57–67.
- Maurer, H.R. and A.G. Green. 1997. Potential coordinate mislocations in crosshole tomography: results from the Grimsel Test Site, Switzerland. *Geophysics*, **62**, 1696–1706.
- McNeill, J. D. 1980. *Electromagnetic terrain conductivity measurements at low induction numbers*. Missisauga, Ont. Geonics Ltd. (Technical Note TN-6.)
- Moorman, B.J., S.D. Robinson and M.M. Burgess. 2003. Imaging periglacial conditions with ground-penetrating radar. *Permafrost Periglac. Process*, **14**(4), 319–329.
- Musil, M., H.R. Maurer, H. Horstmeyer, F.O. Nitsche, D.S. Vonder Mühll and A.G. Green. 2002. High-resolution measurements on an Alpine rock glacier. *Geophysics*, **67**(6), 1701–1710.
- Musil, M., H.R. Maurer, K. Holliger and A.G. Green. 2006. Internal structure of an alpine rock glacier based on crosshole georadar traveltimes and amplitudes. *Geophys. Prospect.*, **54**, 273–285.
- Nabighian, M.N. and J.C. Macnae. 1987. Time domain electromagnetic prospecting methods. In Nabighian, M.N., ed. *Electromagnetic methods in applied geophysics*. Tulsa, OK, Society of Exploration Geophysicists.
- Newman, G.A. and D.L. Alumbaugh. 1997. Three-dimensional massively parallel electromagnetic inversion – 1. Theory. *Geophys. J. Int.*, **128**, 345–354.
- Noetzli, J., M. Hoelzle and W. Haeblerli. 2003. Mountain permafrost and recent Alpine rock-fall events: a GIS-based approach to determine critical factors. In *8th International Conference on Permafrost, 21–25 July 2003, Zürich, Switzerland. Proceedings*. Lisse, etc. A.A. Balkema 827–832.
- Palmer, D. 1980. *The generalized reciprocal method of seismic refraction interpretation*. Tulsa, OK, Society of Exploration Geophysicists. (Report 104.)
- Reynolds, J.M. 1997. *An introduction to applied and environmental geophysics*. Chichester, John Wiley and Sons.
- Streich, R., J. van der Kruk and A.G. Green. 2006. Three-dimensional multicomponent georadar imaging of sedimentary structures. *Near Surf. Geophys.*, **4**, 39–48.
- Stummer, P., H.R. Maurer, H. Horstmeyer and A.G. Green. 2002. Optimization of DC resistivity data acquisition: real-time experiment design and a new multi-electrode system. *IEEE Trans. Geosci. Remote Sens.*, **40**(12), 2727–2736.
- Todd, B.J. and S.R. Dallimore. 1998. Electromagnetical and geological transect across permafrost terrain, Mackenzie River delta, Canada. *Geophysics*, **63**(6), 1914–1924.
- Van der Veen, M., H. Buess, F. Büker and A.G. Green. 2000. Evaluation of high-frequency sources for imaging shallow structures. *J. Environ. Eng. Geophys.*, **5**, 39–56.
- Vonder Mühll, D.S. and P. Holub. 1992. Borehole logging in Alpine permafrost, Upper Engadine, Swiss Alps. *Permafrost Periglac. Process*, **3**(2), 125–132.
- Vonder Mühll, D.S. and 7 others. 2005. Permafrost der Schweizer Alpen 2002/03 und 2003/04. *Die Alpen*, **81**(10), 24–31.
- Zelt, C.A. and R.B. Smith. 1992. Seismic traveltimes inversion for 2D crustal velocity structure. *Geophys. J. Int.*, **108**, 16–34.

MS received 4 May 2006 and accepted in revised form 3 October 2006